Journal of Materials Chemistry A

ROYAL SOCIETY OF CHEMISTRY

PAPER

View Article Online
View Journal | View Issue

Cite this: J. Mater. Chem. A, 2020, 8, 4950

Achieving high-energy dual carbon Li-ion capacitors with unique low- and high-temperature performance from spent Li-ion batteries†

M. L. Divya,[a] Subramanian Natarajan,[a] Yun-Sung Lee *[b] and Vanchiappan Aravindan *[a]

Received 19th December 2019
Accepted 8th February 2020

DOI: 10.1039/c9ta13913c

rsc.li/materials-a

Graphite, an ordered layered structure, has been the dominant choice as a stable electrode material since the commercialization of lithium-ion batteries (LIBs), which could bring about a significant increase in demand for the material owing to its usage in forthcoming graphite-based energy storage devices. In this work, we propose an efficient route to reutilize recovered graphite (RG) from spent LIBs as an anode material for the fabrication of lithium-ion capacitors (LICs) after the required treatment. It was found that RG displayed a first excellent performance in a half-cell configuration, which further encouraged us to assemble a full cell using activated carbon as the cathode. Prior to the fabrication of the LIC, the RG was pre-lithiated (LiC_6) to form a graphite intercalation compound to supply Li ions. The resultant dual-carbon LIC in an aprotic organic solvent delivered a maximum energy density of 185.54 W h kg^{-1} at a power density of 0.319 kW kg^{-1} at ambient conditions. Furthermore, different temperature performance analysis revealed that the assembled LIC presented a good cycling performance for a continuous 2000 cycles with ~75% capacity retention at 10 °C and 25 °C. The developed dual carbon-based LIC using recovered RG from spent LIBs offers several promising features, such as low cost and good applicability in a wide range of temperature operations as well as providing a real solution to recycle the upcoming massive quantity of spent LIBs generated by different electronic appliances.

1. Introduction

Lithium-ion capacitors (LICs) are generally branded in terms of a burgeoning energy storage device as they show mid-performance between lithium-ion batteries (LIB) and electrical double-layer capacitors (EDLC) by presenting high energy and power density.[1–3] Generally, LICs are fabricated with a high-capacity battery-type electrode and high-rate capacitor-type electrode in combination with an appropriate electrolyte, mostly Li salt in an organic solvent. The charge-storage process in LICs occurs due to ionic adsorption and desorption on the EDLC electrode and lithium (Li^+) intercalation/de-intercalation in a battery-type electrode.[3,4] Typically, LIBs can achieve high energy density (150–200 W h kg^{-1}) in an organic electrolyte system with a low power density (<1000 W kg^{-1}) and short life-span. On the other hand, supercapacitors/EDLC-type electrodes can exhibit a high power capability (>10 kW kg^{-1}) and long life-span with a low energy density (5–10 W h kg^{-1}). Hence, the LIC is a smart configuration where the boundaries of both LIBs and EDLCs can be overwhelmed to realize a high energy density and high power capability in a single system. Based on the type of electrode materials, LICs can be categorized into dual carbon (DC), non-carbon, and hybrid LICs.[5] Among the two carbon electrodes, one undergoes a perfect faradaic reaction, whereas the others involve non-faradaic processes.

The performance of an LIC mainly depends on the type of electrode materials, electrolytes, and also the operating voltage window. Carbon materials are widely used as the electrode material for LICs due to many factors, like their low cost, ease of tailoring the specific surface area, sizeable potential window, high conductivity, and exceptional electrolyte friendliness.[4,6,7] Generally, DC-LICs possessing both carbon electrodes are the most encouraging type of LICs due to their low cost and better cyclic stability compared with other LICs possessing a metal-containing insertion-type[8] or alloy/conversion-type negative electrodes.[3,5] However, the attractiveness of the LIC concept is marred by the absence of a lithium source in the electrodes of the devices as Li^+ ions are mainly derived from the electrolyte. Also, the irreversible formation of a solid electrolyte interface (SEI) film on the negative electrode during the cycling of the system will consume the available Li^+ ions, which makes it

[a]Department of Chemistry, Indian Institute of Science Education and Research (IISER), Tirupati 517507, India. E-mail: aravind_van@yahoo.com

[b]Department of Advanced Chemicals and Engineering, Chonnam National University, Gwang-ju 61186, Republic of Korea. E-mail: leeys@chonnam.ac.kr

† Electronic supplementary information (ESI) available: Experimental section, XPS spectra, half-cell performance of AC, DC-LIC performance at various temperatures, comparison of four duplicate DC-LICs, and cycling profiles along with the impedance spectra. See DOI: 10.1039/c9ta13913c

necessary to perform pre-lithiation for the negative electrode before LIC fabrication.[1,2] DC-LICs can be assembled with a double-layer capacitive carbon as the positive electrode and pre-lithiated carbon as the negative electrode using an organic electrolyte solution.[5] Long-range-ordered carbonaceous materials can directly act as battery-type negative electrode in LICs as they contain active sites for Li^+ intercalation and de-intercalation.[9] During the diffusion-controlled charge–discharge process, the faradaic reaction on the negative electrode typically retains a constant potential, while for the capacitor-type positive electrode (*e.g.*, activated carbon, AC) the voltage varies linearly with the charge–discharge time. For the DC-LIC system, the energy density depends on the specific capacity of the battery-type electrode, and the power density is influenced by the type of capacitor-type electrode.[5]

Long-range-ordered carbonaceous materials can be considered as a prospective anode for DC-LICs[10–13] owing to their nearly flat Li-intercalation/de-intercalation profile at a low redox negative potential (~0.1 V *vs.* Li) and high theoretical capacity (372 mA h g^{-1}). In general, graphite can be obtained either artificially (synthetically produced) or naturally (mined from the ground). Based on the purity and morphology, natural graphite is further classified into three types: amorphous, flake, and vein graphite. The long-range ordering of graphite material is essential for the faradaic reaction; however, the graphite should also be in a highly pure and well-crystallized state. Therefore, only flake and vein graphite can be used as a raw material for the anode in LIBs or LICs due to their high degree of graphitization. Mostly, flake graphite is available in a ~75–97% pure and highly crystallized form. Due to the limited sources of vein graphite in a few countries, vein graphite may fail to find a place in energy applications in the future. Hence, LIB/LIC-grade graphite is not abundant enough to be considered as a source of raw material for future energy applications.[14]

The recycling and reuse of spent LIB materials have become practical solutions to manage the rising demand for raw materials to manufacture new LIBs for various applications as well as to avoid environmental issues.[15–19] The direct disposal of spent LIBs is a menace to human health and the environment due to the presence of hazardous constituents in the LIBs. However, spent LIBs can be recycled to regain the valuable components efficiently, which can then be reused for energy storage devices as well as for other applications.[20–22] Presently, graphite is the state-of-the-art anode material for the majority of commercial LIBs. As a result, graphite's market value is predicted to reach around $27.03 billion by 2025, and indeed graphite demand could increase in the future since 125 million electric vehicles are anticipated to run globally by that time.[23] By weight, graphite is ~12–21% of the LIB (representing the second-largest component), which is nearly 10–15% more than lithium. Also, it should be noted that the large EV battery has ~25 kg of graphite in each LIB anode. The demand for graphite will surge in the coming years to meet the demand from fast-growing energy applications, like in electric vehicles, that will use efficient energy storage devices, such as LIBs and LICs, in the future.[24,25] On the other hand, along with the mounting demand for LIBs, the number of spent LIBs will also increase in the e-waste stream, which could lead to a tremendous amount of waste graphite.[26–28] Therefore, there is an opportunity to reuse the waste sourced from spent LIBs, which offers paybacks of improving environmental protection and making it a more cost-effective process. In this study, we attempted to recover graphite material from mixed spent LIBs used in mobile phones by ultrasonic leaching, which is a simple solid–liquid extraction method, and to explore the possibility of using this recovered graphite (RG) as a battery-type electrode material for an LIC. The compositional and structural characterization of RG was studied with various analytical tools and the electrochemical characterization was performed in both half-cell and LIC configurations. In order to ensure our results and to check their reproducibility, we made three duplicate cells and compared the results. Further, we investigated the low- and high-temperature performances of the fabricated LIC and recorded the results.

2. Experimental section

2.1. Recovery and utilization of graphite from spent Li-ion batteries

The spent LIBs from the collected mobile phones were submerged in NaCl solution for one day irrespective of the model or manufacturer to allow them to discharge completely so as to circumvent any hazards while dismantling the batteries. The current collector Al-foil containing the Li-based metal oxide and the separator were separated from the anode (Cu-foil holding graphite paste) and stored for later reuse for energy applications. First, the loosely-bounded graphite paste was separated from the Cu foil *via* a simple sonication method using de-ionized water to collect "Li" that was on the anode part due to the solid-electrolyte interphase formation during the charge–discharge process. Subsequently, any unrecovered graphite that was hard to remove was treated with dimethylformamide (DMF) solvent to separate out entirely from the Cu foil. After centrifugation, the DMF-treated graphite was further washed with de-ionized water and heated at 800 °C for 3 h under an Ar atmosphere.

2.2. Physical characterization

The heat-treated graphite material from the spent LIBs was subjected to powder X-ray diffraction (XRD, ULTIMA-IV, Rigaku, ARBL-RAD) and Raman spectroscopy (LabRam HR800 UV Raman microscope, Horiba Jobin-Yvon, France) to study the purity, structural properties, crystallinity, and phase of the material. The XRD analysis was done with monochromatic Cu Kα radiation (λ = 0.15406 nm) at a scanning rate of 1° min^{-1}. Raman spectra of the material were recorded at room temperature using a 515 nm diode laser as an excitation light source. X-ray photoelectron spectroscopy (XPS, Multilab 2000, UK) was performed to ensure the presence of different surface functional groups and heteroatoms on the surface of the material. The surface morphology and internal structure of the material were investigated with scanning electron microscopy (SEM S-

4700, Hitachi, Japan) and high-resolution transmission electron microscopy (HR-TEM, JEM-2000, EX-II, JEOL, Japan).

2.3. Electrode preparation and measurement

To evaluate the electrochemical performance of the recovered graphite (RG), the half-cell performance was studied in a coin cell (CR 2016) assembly with Li metal as the counter electrode and a reference electrode. The RG electrodes were prepared by mixing the active material, conductive carbon (Super-P), and polyvinylidene fluoride (PVdF) binder in the ratio of 80 : 10 : 10 using *N*-methyl pyrrolidone (NMP) solvent. The slurry was mixed under constant stirring for a period of 6 h to get a uniform dissolution and further it was cast on to a ~0.02 mm thickness Cu-foil using a doctor blade. The slurry-coated Cu-foils were dried overnight, and the dried foils were pressed under a hot roll press (Tester Sangyo, Japan). Disc electrodes with a diameter of 14 mm were cut out and it was noted that the mass of active material in each disc was within the range of ~3 mg. Similarly, activated carbon (AC, YP 80F, surface area: 2100 m^2 g^{-1}, pore volume: 0.97 ml g^{-1}, Kuraray, Japan) electrodes were prepared by mixing the active material, conductive carbon (Super-P), and teflonized acetylene black (TAB-2) binder in the weight ratio of 80 : 10 : 10 using ethanol as the solvent. The electrode material was pressed on a 16 mm diameter stainless steel mesh current collector (Goodfellow, UK) and the electrodes were dried at 75 °C in a vacuum oven for 4 h. Subsequently, half-cells were fabricated in an Ar-filled glove box using 1 M $LiPF_6$ electrolyte (ethylene carbonate (EC): dimethyl carbonate (DMC), 1 : 1 v/v, Tomiyama, Japan), with Whatman paper (1825-047, GF/F) used as the separator for both electrodes at a current rate of 100 mA g^{-1}. Electrochemical impedance spectroscopy (EIS) and galvanostatic charge–discharge studies were performed for both (Li/RG and Li/AC) half cells with a battery tester (Biologic, France) to check the capability of these electrodes as the anode and cathode for LIC assembly.

2.4. LIC fabrication and performance analysis

LICs were fabricated in coin cell (CR 2016) assemblies with pre-lithiated RG (LiC_6) and employed as the anode and AC electrode as the cathode under balanced mass-loading conditions with a Whatman separator and 1 M $LiPF_6$ in EC:DMC as the electrolyte. First, the RG electrode was pre-lithiated in the half-cell configuration (Li/RG) using a Swagelok assembly at a constant current density of 100 mA g^{-1}. Briefly, the cell was first discharged to 0.005 V *vs.* Li, followed by two complete charge–discharge cycles (2–0.005 V *vs.* Li) to yield the lithiated phase (LiC_6). The AC electrodes were formulated with a balanced mass of active material to compensate for the discharge capacity of the LiC_6 phase. The electrochemical properties of the AC/LiC_6-based LICs were analyzed through galvanostatic charge–discharge studies (1.8–4.3 V) at various current densities of 0.1 to 2.5 A g^{-1}, and also by EIS measurements. For all the fabricated LICs, the energy and power densities were calculated based on the total mass of active material in both the electrodes. Most importantly, the low- and high-temperature performances

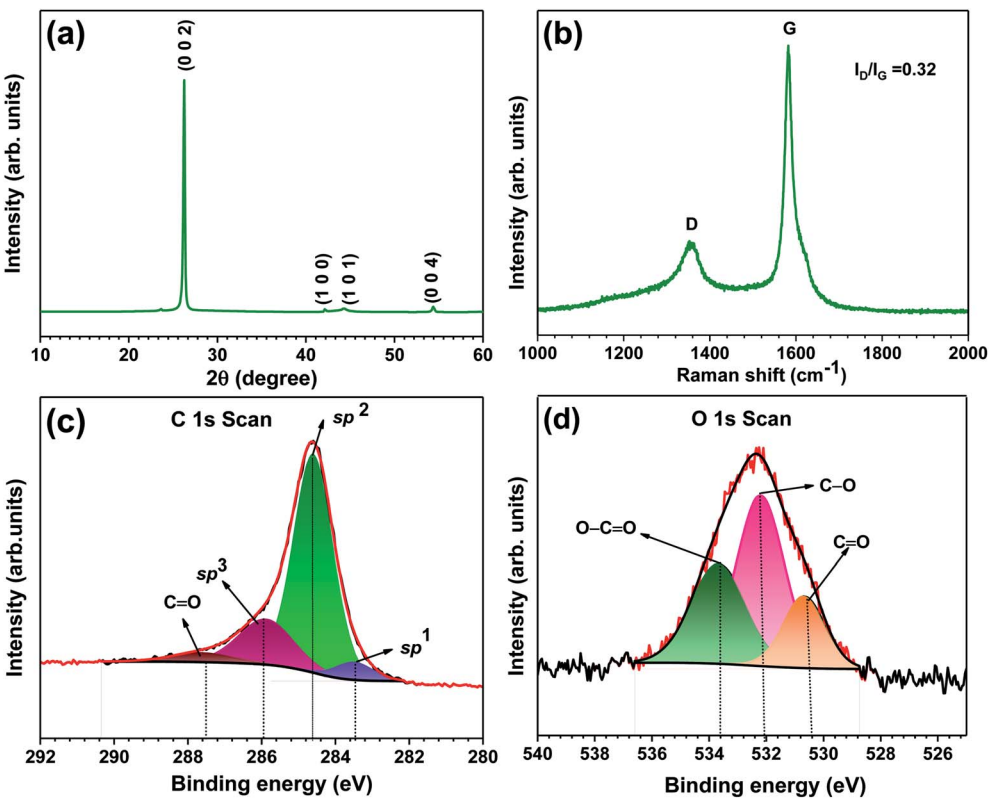

Fig. 1 Physical characterization of RG: (a) XRD pattern, (b) Raman spectrum, (c and d) XPS spectra: (c) C 1s scan, and (d) O 1s scan.

of these LICs were investigated using the environmental chamber (Espec, Japan).

3. Results and discussion

The X-ray diffraction (XRD) pattern of RG is illustrated in Fig. 1a, showing a sharp diffraction peak at 26.24° conforming to the (002) plane and agreeing with the hexagonal phase with the space group $P6_3mc$. Further, the peaks positioned at 42.17°, 44.10°, and 54.38° correspond to the (100), (101), and (004) planes, respectively. The Raman spectrum of the RG is given in Fig. 1b to elucidate the structural features of the recovered carbon material from the spent LIBs. As expected, the spectrum clearly shows the characteristic D and G bands at ~1363 and ~1582 cm^{-1}, respectively. Also, the RG intensity ratio of the D and G bands was calculated as 0.32, indicating the presence of fewer structural defects and invisible edge distortion in the graphite structure. It is well known that the appearance of the G band is mainly due to in-plane vibrations of sp^2 carbon atoms, whereas the D band is due to the presence of amorphous carbon with sp^3 carbon atoms.[29–31]

X-ray photoelectron spectroscopy (XPS) was carried out to understand the surface functionalities and the presence of defects in RG and the spectra can be seen in Fig. 1c and d. The presence of different surface functional groups on the RG sample was revealed by the raw spectra of the recovered graphite[32] (Fig. S_1†), which indicates the presence of C and O functionalities. The de-convolution spectra of C 1s confirmed the C–C stretching in the recovered graphite by displaying a sharp peak at the binding energy of ~284.7 eV. The binding energies of 286.0, 287.5 and 283.2 eV, correspond to sp^3 carbon, carbonyl carbon (C=O), and sp^1 carbon or peaks due to metal impurities, respectively. The O 1s was composed of three prominent regions positioned at the binding energies of ~530.5, ~532, and ~533.5 eV for C=O, C–O, and O–C=O environments, respectively. The observed XPS spectra clearly suggest that the RG exhibited similar surface features as commercial graphite and no by-products were found on the surface.

The scanning electron microscopy (SEM) images of the RG are presented in Fig. 2a and b, revealing the morphology of the recovered graphite. The flaky kind of surface morphology was observed and also it could be noticed that the surface features were similar to natural flake graphite (NFG). In general, flake-like graphite is considered to be one of the purest forms of graphite with a high degree of crystallinity and it is employed in most commercial LIBs. The HR-TEM pictures of RG confirmed the presence of a layered structure (multilayer graphene) with clear lattice fringes and also detected the interlayer spacing of ~0.352 nm, which corresponds to the (002) plane (Fig. 2d and e). However, the observed *d*-spacing was slightly larger than the normal graphitic phase (0.339 nm), mainly because the continuous Li-ion insertion and extraction process between the Li-based metal oxide and the graphite layers could expand the interlayer spacing of the recovered graphite material. Most importantly, the TEM image clearly showed that the products formed by the electrolyte decomposition were efficiently

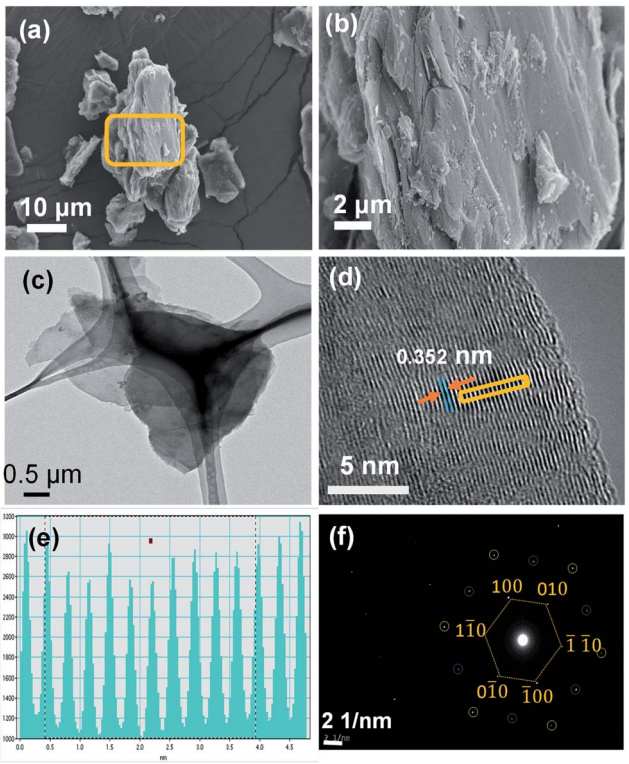

Fig. 2 (a and b) Surface morphology features of RG: (c) TEM picture, (d) HR-TEM images with lattice fringes, (e) line profile of the marked section, (f) SAED pattern of the RG sample.

removed in the recovered graphite during the washing process. Further, the lattice orientations of multilayer graphene were analyzed by electron diffraction in TEM,[33] which showed hexagonal patterns with bright spots in a triangular geometry, representing the AB stacking of graphene layers[34–36] (Fig. 2f). The shift in the angle between two adjacent hexagonal rings was ~28–30°. Hence, it could be understood that the recovered graphite sample still preserved its hexagonal crystal structure with AB stacking, but had a marginally expanded interlayer space in-between the adjacent graphene layers.

To employ RG as a potential insertion host in the fabrication of a high-performance DC-LIC, assessment of the Li-insertion properties is desperately needed. Therefore, the Li-storage properties were assessed in a half-cell configuration (Li/RG) at a current density of 0.1 A g^{-1}, which delivered capacities of ~391 and 330 mA h g^{-1} for the first discharge and charge process, respectively (Fig. 3a). The coulombic efficiency in the first cycle was calculated to be ~84.4% and was consistent with that of commercial graphite, which clearly showed that RG could maintain its structural integrity upon repeated *n*-number of charge–discharge cycles during the "first-life" in the LIB assembly. The first discharge capacity of RG was higher than the theoretical limitation (372 mA h g^{-1}), which was mainly due to the decomposition of the electrolyte solution. The decomposition process consumed the Li in an irreversible manner and formed a surface film (*i.e.*, solid electrolyte interphase) over the graphitic anode surface. As mentioned, the formation of the

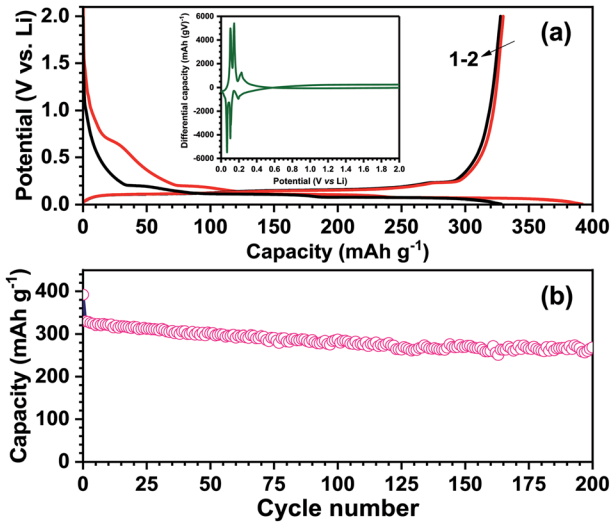

Fig. 3 Half-cell performance of Li/RG cell: (a) galvanostatic charge–discharge profile of RG at a current density of 0.1 A g^{-1}, first (red) and second cycle (black). Inset: differential capacity profile, and (b) cycling profile.

solid electrolyte interphase is also essential for the safe operation of the graphitic anode, since LiC_6 is considered to be a strong reducing agent, which could further reduce the electrolyte solution. Hence, appropriate protection is necessary to prevent the inevitable side reactions. Further, a well-formed SEI layer is beneficial for the betterment of the cell, since it could exhibit high Li-ion conductivity, allow the permeation of only Li-ions into graphite, prevent the solvent molecules co-intercalation, and could also avoid further reduction of the electrolyte. On the other hand, in Li-intercalation into graphite, Li-ions diffuse in the in-plane direction and settle in the sites between the two graphene planes, which is at the center of the hexagonal carbon (C) rings along the *c*-axis (LiC_6) and can deliver a theoretical capacity of ~372 mA h g^{-1}.[37] More clearly, Li-intercalation into graphite is a staging process; therefore in order to probe such a process, differential capacity profiles were derived from the charge–discharge curves (inset, Fig. 3a). The presence of multiple derivative peaks at lower potentials, specifically <0.2 V *vs.* Li, correspond to the formation of staged nano-scale intercalation compounds (Li_xC_6) from stage 4, stage 3, stage 2, and stage 1. The cyclic stability of the RG electrode was also studied and showed ~68.38% retention after 200 cycles (Fig. 3b). To compare the performance of RG with commercially available graphite, the first charge–discharge curves of both materials are given in Fig. S_2.†

Unlike the symmetric supercapacitors, in the hybrid configuration, both electrodes undergo different charge-storage mechanisms; for example, RG obeys the faradaic behavior, whereas a non-faradaic behavior is noted for the counter electrode AC. Therefore, mass balance is very crucial for the assembly, since the charge-storage capability depends on the individual electrodes. Hence, AC was subjected to a study of its half-cell performance (Li/AC) to assess the physisorption process under the same current rate (0.1 A g^{-1}). The cell exhibited an initial discharge capacity of 95 mA h g^{-1} with a capacity retention of ~94% after 100 cycles (Fig. S_3 and S_4†). The linear charge–discharge profiles without any prominent plateaus represent the accumulation of the charge carriers in the surface of the AC electrode. It was indicated that the AC demonstrated a purely a non-faradaic behavior, *i.e.*, adsorption and desorption of ions on the surface and a subsequent double-layer formation. The anion PF_6^- in the Li-based electrolyte was not only involved in the formation of a double-layer across the interface but also the cation Li^+ was involved in such a process.[38] Consequently, the charge carriers, especially Li^+, present in the electrolyte were not sufficient to realize the higher energy density. To supply a sufficient amount of Li, pre-lithiation of the battery type electrode is one of the efficient ways to fulfill this requirement. Accordingly, the RG was pre-lithiated (LiC_6) in a Swagelok assembly by way of constructing a half-cell configuration.

The DC-LIC was fabricated with a pre-lithiated RG (LiC_6) electrode as the anode, AC electrode as the cathode, and 1 M $LiPF_6$ in EC:DMC as the electrolyte. Briefly, in the pre-lithiation, the half-cell was subjected to two complete discharge–charge cycles followed by a third discharge, and then it was dismantled and paired with the AC electrode. The specific capacity of both electrodes was balanced by considering the second discharge capacity of the AC electrode and the final discharge capacity (3rd discharge) of the pre-lithiated graphite electrode (LiC_6). The LIC was fabricated with a mass loading of graphite to AC in the ratio of ~4.04 to balance their capacities.[39] In terms of weight, the total mass of active material was 11.258 mg (2.232 mg RG + 9.026 mg AC). The fabricated LIC displayed an open circuit potential (OCV) of ~2.9 V. The charge–discharge profile of the assembled LICs was tested at different current rates ranging from 0.1 to 2.5 A g^{-1} within the potential window of 1.8–4.3 V at room temperature. It should be noted that the total active mass of the electrode was taken into consideration for the calculation of the current density. Upon charging, the PF_6^- ions and partially the Li^+ ions in the electrolytes migrate toward the positive AC electrode and tend to form an electric double layer on the surface, whereas the Li^+ ions are intercalated into the gap between the graphene layers. During discharging, the ions will migrate in the opposite direction, and Li-deintercalation takes place from the graphite.[39] The involvement of two different charge–storage mechanisms in LIC was supported by the CV traces, in which a clear distortion from the rectangular-shaped curve was observed (Fig. S_5†). The energy and power density values were calculated based on the total mass of active material in both the electrodes. The energy density values of LICs were obtained by multiplying the specific capacity value with the intersecting voltage, *i.e.*, working potential, and the corresponding power density values were obtained by dividing the energy density values with the discharge time (ESI†). A more or less linear charge–discharge profile was obtained at room temperature irrespective of the applied current densities (Fig. 4a). The linearity was mainly due to the lower polarization offered by the battery-type electrode, LiC_6 (Fig. 4b). As a result, the linear behavior of the AC did not deviate much. The AC/LiC_6-based DC-LIC exhibited a maximum

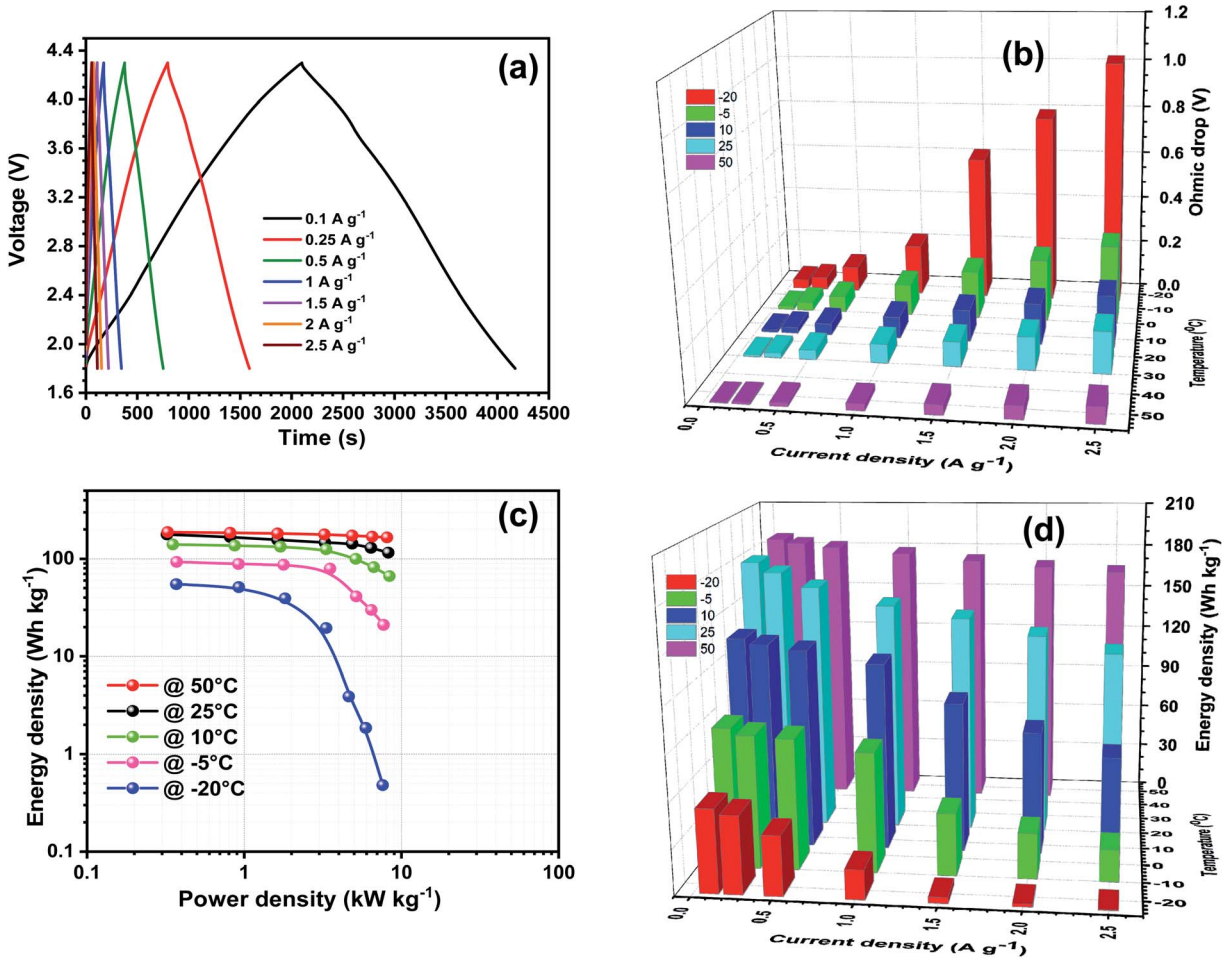

Fig. 4 Electrochemical performance of the assembled DC-LIC: (a) voltage *vs.* time profile for the DC-LIC at 25 °C for varying current rates of 0.1–2.5 A g^{-1}, (b) 3D plot showing the increase in ohmic drop values with the decrease in temperature for the assembled LIC at different current rates, (c) Ragone plot representing the energy power density values of the DC-LIC at different temperatures, and (d) 3D plot showing the change in energy density values of the DC-LIC with temperature for different current density values.

energy density of 185.5 W h kg^{-1} at a power of 0.319 kW kg^{-1} at room temperature.

To study the temperature-dependent performance of the DC-LIC, a duplicate cell was fabricated and subjected to various atmospheric conditions using the environmental chamber. Prior to the study of the electrochemical activity of the duplicate cell in various environments, the room temperature performance was tested to ensure the reproducibility of the above-mentioned energy. Accordingly, four different duplicate DC-LICs were tested at room temperature, showing a mean value of 180.67 W h kg^{-1} with a standard deviation of ~5 W h kg^{-1} at a low current rate (0.1 A g^{-1}, Fig. S_6†). This clearly indicated the excellent re-reproducibility of our work, which was mainly due to the appropriate optimization of mass loading, controlled pre-lithiation, fixed potential window, and unquestionably the inherent performance of the individual electrodes. Further, a high-temperature study was carried out at 50 °C and it was observed that there was not much difference in the charge–discharge profiles because of the increased activity of electrolyte with the electrode (Fig. S_7†). As expected, reduced polarization was noted for the high-temperature operation of the cell. The DC-LIC displayed a maximum energy density of 187.75 W h kg^{-1} at a power density of 0.33 kW kg^{-1} at 50 °C. Even at a high power density (8.1 kW kg^{-1}), the LIC exhibited an energy density of 165.87 W h kg^{-1}, which is one of the best values reported for DC-LICs (Table S_1†). We strongly believe that the high energy density of the LIC was because of the combined features of both the cathode and anode materials with the balanced mass loading, while the high specific surface area and abundant pores are the most crucial parameters and create more active sites for ion adsorption. Interestingly, in the case of RG, the expansion of interlayer spacing (0.352 nm) after annealing could help to achieve the high electrochemical performance *via* facilitating the fast Li^+ intercalation/de-intercalation process at higher rates. On the other hand, completely different and unique profiles were observed at low-temperature conditions (10, −5 °C and −20 °C). The deviation in the linear charge–discharge profiles was disturbed with the decrease in temperature. Hence, the DC-LIC's low-temperature profiles were different from those under high and room temperature

conditions (Fig. S_7†). This distortion in the charge–discharge profiles was due to sluggish faradaic reactions offered by the battery-type electrode, RG.[10] As a result, a dramatic increase in the ohmic drop/polarization was evident in the low-temperature operation compared to in the elevated state (Fig. 4b).

A Ragone plot is one of the best ways to represent the energy and power density relationship and such a graph was plotted for the fabricated LIC (Fig. 4c) in this study. The DC-LIC displayed maximum energy densities of 140.5, 93.0, and 55.0 W h kg^{-1} and minima of 66.6, 21.1, and 0.48 W h kg^{-1} for the temperatures 10 °C, −5 °C, and −20 °C, respectively. The energy storage capacity of the AC/LiC_6-based LIC was superior to that of previously reported similar dual carbon-based systems.[12,40–43] Additionally, the effect of temperature on the performance of the DC-LIC was described in the form of 3D plots (Fig. 4b and d). Apparently, the DC-LIC displayed a very high energy density at elevated temperature conditions of 50 °C regardless of the applied current rates. However, the energy density values started falling when decreasing the temperature and the applied current rate. Also, the performance was worse for high current densities, especially for the case at −20 °C at a current density of 2.5 A g^{-1} and this poor performance was mainly associated with the increased cell polarization originating from the sluggish Li-ion kinetics under low-temperature operation (because of the increase in the solution resistance, as supported by the impedance studies). Generally, under low-temperature conditions (−5 °C and −20 °C), the electrolyte solution is crystallized, thus hindering the mobility of Li^+ ions, which eventually affects the ionic conductivity. Also, this leads to a rise in the charge-transfer resistance and polarization, which results in the decreased electrochemical performance. However, it should be noted that graphite is well known for its worse electrochemical performance under sub-zero temperature conditions.

Cyclic stability is another important factor in validating the potential use of a charge-storage system regardless of the mechanism and configuration. Cycling studies were thus performed at various current densities and temperature conditions. It has been well established that graphite is the best insertion host for low-power applications. Accordingly, the DC-LIC was subjected to different current rates from 0.25 to 1 A g^{-1} for limited cycles (Fig. S_8a†). The LIC exhibited capacity retentions of ~81%, 85%, and 75% for the current densities of 0.25, 0.5, and 1 A g^{-1}, respectively. Obviously, an inferior performance was noted at the higher current rate, which led us to limit the further studies to be performed at 0.5 A g^{-1} only for the assembled DC-LICs. After the fabrication of fresh cells, the DC-LICs were cycled five times at 25 °C, followed by 2000 cycles at various temperature conditions of −5 °C, 5 °C, 10 °C, 25 °C, and 50 °C (Fig. 5a). Interesting cycling profiles were registered for the different temperature conditions; for example, the cell exhibited moderate cycling stability at 25 °C and 10 °C with a capacity retention of >75%. Also, a much worse performance was noted for the low-temperature conditions (−5 °C), while almost the same behavior was reflected at an elevated condition of 50 °C. Interestingly, deterioration was noted at up to 50 cycles in all the cases, which indicates that the DC-LIC requires extended formation cycles to exhibit a stable performance.

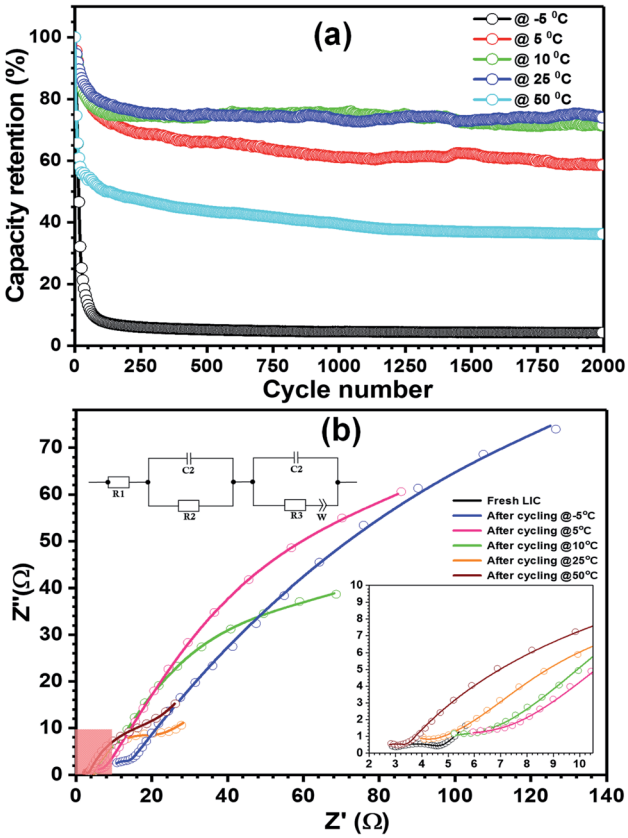

Fig. 5 (a) Cyclic performance of the DC-LIC at different temperatures, and (b) Nyquist plots for the EIS analysis for the assembled DC-LIC before and after cycling, in which the circles relate to the experimental data and the lines corresponds to the fitting values.

In order to gain further insights into the charge-storage behavior of the systems, EIS measurements were further examined for both the half-cell (Fig. S_8b†) and full-cell configurations (Fig. 5b). The EIS data were generated in the frequency range of 10 kHz to 1 Hz by applying an amplitude of 10 mV to decrease perturbation of the system. For the fresh Li/AC half-cell, the Nyquist plot showed a semicircle in the high to medium frequency range with a short low-frequency tail. However in the case of the fresh Li/RG half-cell, the diameter of the semicircle was comparatively less, its low-frequency straight line was steeper than 45°. Generally, in the high-frequency region, EIS forms a small curve, which indicates the ohmic resistance and inductance of a cell. The high-to-middle-frequency part of the EIS results showed an arc, which is a result of the solution resistance and charge transfer at the electrode surface. The straight-line with a constant slope (Warburg type) at the low-frequency region of the EIS represents the phenomenon of Li^+-ion diffusion. A straight line with a 45° slope corresponds to semi-infinite diffusion.[44,45] However, the Nyquist plot of DC-LIC was different from that of LIB, such that the arc present in the high-to-middle-frequency region typically did not arise in the case of DC-LIC. The shape of the Nyquist plot of DC-LIC was generally similar to that of the EDLCs except for the slightly higher impedance as in the case of LIB, which could be due to the pre-lithiated negative electrode of DC-LIC.

The Nyquist plots were recorded for the fresh as well as cycled LICs at different temperatures of −5 °C, 5 °C, 10 °C, 25 °C, and 50 °C. The plots of fresh LIC showed a single depressed semicircle in the high-to-medium-frequency region, with a Warburg tail in the low-frequency region. However, the plot of DC-LIC after the pre-lithiation process possessed a small arc in the high-frequency area, which indicates impedance of the SEI layer formation on the surface of the LiC_6 electrode.[46] The plots illustrate that with a decrease in temperature, the impedance becomes more extensive in the low-frequency region. In the high-frequency region, the impedance at different temperatures coincides with each other, and this portion of the graph has been enlarged for a clearer view, which overall indicates that the effect of temperature on the performance of LIC was based only on the rate of diffusion and the charge-transfer mechanism in the electrode–electrolyte interface. The large Warburg tail in the low-frequency region at low temperature represents a slow diffusion of ions,[47] while the variation in the diameter of the semicircle in the high-to-medium-frequency region during cycling indicates the change in resistance of Li^+ ions drives them through the SEI film formed.[18]

4. Conclusion

In this study, we proposed a simple, cost-effective, and environmentally friendly approach to reutilize the recovered graphite (RG) from spent LIBs as an anode material for the fabrication of high-energy-density dual-carbon Li-ion capacitors. The fabricated DC-LIC-based regenerated graphite exhibited a maximum energy density value of 185.54 W h kg^{-1} at room temperature and demonstrated superior performance compared to the values reported for previously studied dual-carbon hybrid systems. Further, the high- and low-temperature performances of DC-LIC were also investigated to investigate the possibility of using the fabricated DC-LIC in different environmental conditions. From these results, it was proved that the mended graphite revived the pathway for efficient Li^+ transport through this proposed simple treatment to achieve a high-performance LIC. Moreover, this study envisages the possibility of using recovered graphite as a worthy electrode material for the fabrication of various high-energy-storage devices and also would be beneficial for the environment under the "waste-to-wealth" approach.

Conflicts of interest

There are no conflicts to declare.

Acknowledgements

MLD wishes to thank the funding through Women Scientist Scheme-B (DST/WOS-B/2018/2039) from the KIRAN division of the Department of Science & Technology (DST), Govt. of India. VA also acknowledges financial support from the Science & Engineering Research Board (SERB), a statutory body of the DST, Govt. of India, through the Ramanujan Fellowship (SB/S2/RJN-088/2016). YSL acknowledges the financial support from the National Research Foundation of Korea (NRF) grant funded by the Korea government (Ministry of Science, ICT & Future Planning) (No. 2019R1A4A2001527).

References

1 P. Jeżowski, O. Crosnier, E. Deunf, P. Poizot, F. Béguin and T. Brousse, Safe and recyclable lithium-ion capacitors using sacrificial organic lithium salt, *Nat. Mater.*, 2017, **17**, 167.
2 X. Sun, W. Chen, X. Li, J. Wang, H. Hu, G. Liang, Y. Huang and C. Wei, Performance and Applications of Lithium Ion Capacitors, in *Science, Technology and Advanced Application of Supercapacitors*, IntechOpen, 2018.
3 V. Aravindan and Y.-S. Lee, Building Next-Generation Li-ion Capacitors with High Energy: An Approach beyond Intercalation, *J. Phys. Chem. Lett.*, 2018, 3946–3958.
4 X. Wang, L. Liu and Z. Niu, Carbon-based materials for lithium-ion capacitors, *Mater. Chem. Front.*, 2019, **3**(7), 1265–1279.
5 G. Li, Z. Yang, Z. Yin, H. Guo, Z. Wang, G. Yan, Y. Liu, L. jun Li and J. Wang, A review on non-aqueous dual-carbon lithium-ion capacitors, *J. Mater. Chem. A*, 2019, **7**(26), 15541–15563.
6 R. L. McCreery, Advanced carbon electrode materials for molecular electrochemistry, *Chem. Rev.*, 2008, **108**(7), 2646–2687.
7 F. Sun, J. Gao, Y. Zhu, X. Pi, L. Wang, X. Liu and Y. Qin, A high performance lithium ion capacitor achieved by the integration of a Sn–C anode and a biomass-derived microporous activated carbon cathode, *Sci. Rep.*, 2017, **7**, 40990.
8 V. Aravindan, J. Gnanaraj, Y.-S. Lee and S. Madhavi, Insertion-Type Electrodes for Nonaqueous Li-Ion Capacitors, *Chem. Rev.*, 2014, **114**(23), 11619–11635.
9 X. Wang, L. Liu and Z. Niu, Carbon-based materials for lithium-ion capacitors, *Mater. Chem. Front.*, 2019, **3**(7), 1265–1279.
10 S. Jayaraman, S. Madhavi and V. Aravindan, High energy Li-ion capacitor and battery using graphitic carbon spheres as an insertion host from cooking oil, *J. Mater. Chem. A*, 2018, **6**(7), 3242–3248.
11 S. Jayaraman, A. Jain, M. Ulaganathan, E. Edison, M. P. Srinivasan, R. Balasubramanian, V. Aravindan and S. Madhavi, Li-ion *vs.* Na-ion capacitors: A performance evaluation with coconut shell derived mesoporous carbon and natural plant based hard carbon, *Chem. Eng. J.*, 2017, **316**, 506–513.
12 S. R. Sivakkumar and A. G. Pandolfo, Evaluation of lithium-ion capacitors assembled with pre-lithiated graphite anode and activated carbon cathode, *Electrochim. Acta*, 2012, **65**, 280–287.
13 Y. Li, Y. Lu, P. Adelhelm, M.-M. Titirici and Y.-S. Hu, Intercalation chemistry of graphite: alkali metal ions and beyond, *Chem. Soc. Rev.*, 2019, **48**(17), 4655–4687.

14 X. Gao, C. Zhan, X. Yu, Q. Liang, R. Lv, G. Gai, W. Shen, F. Kang and Z.-H. Huang, A high performance lithium-ion capacitor with both electrodes prepared from Sri Lanka graphite ore, *Materials*, 2017, **10**(4), 414.

15 F. C. McMichael and C. Henderson, Recycling batteries, *IEEE Spectrum*, 1998, **35**(2), 35–42.

16 Z. P. Cano, D. Banham, S. Ye, A. Hintennach, J. Lu, M. Fowler and Z. Chen, Batteries and fuel cells for emerging electric vehicle markets, *Nat. Energy*, 2018, **3**(4), 279–289.

17 W. Lv, Z. Wang, H. Cao, Y. Sun, Y. Zhang and Z. Sun, A Critical Review and Analysis on the Recycling of Spent Lithium-Ion Batteries, *ACS Sustainable Chem. Eng.*, 2018, **6**(2), 1504–1521.

18 B. Moradi and G. G. Botte, Recycling of graphite anodes for the next generation of lithium ion batteries, *J. Appl. Electrochem.*, 2016, **46**(2), 123–148.

19 G. Harper, R. Sommerville, E. Kendrick, L. Driscoll, P. Slater, R. Stolkin, A. Walton, P. Christensen, O. Heidrich, S. Lambert, A. Abbott, K. Ryder, L. Gaines and P. Anderson, Recycling lithium-ion batteries from electric vehicles, *Nature*, 2019, **575**(7781), 75–86.

20 M. Pagliaro and F. Meneguzzo, Lithium battery reusing and recycling: A circular economy insight, *Heliyon*, 2019, **5**(6), e01866.

21 S. Natarajan, D. Shanthana Lakshmi, H. C. Bajaj and D. N. Srivastava, Recovery and utilization of graphite and polymer materials from spent lithium-ion batteries for synthesizing polymer–graphite nanocomposite thin films, *J. Environ. Chem. Eng.*, 2015, **3**(4, Part A), 2538–2545.

22 S. Natarajan and V. Aravindan, Burgeoning Prospects of Spent Lithium-Ion Batteries in Multifarious Applications, *Adv. Energy Mater.*, 2018, **8**(33), 1802303.

23 https://www.globenewswire.com/news-release/2019/05/10/1821952/0/en/Graphite-Market-to-hit-27-03-Billion-by-2025-Analysis-by-Demand-Size-Share-Price-Growth-Drivers-and-Business-Opportunities-Adroit-Market-Research.html.

24 A. Mayyas, D. Steward and M. Mann, The case for recycling: Overview and challenges in the material supply chain for automotive li-ion batteries, *Sustainable Mater. Technol.*, 2019, **19**, e00087.

25 Y. Yang, S. Song, S. Lei, W. Sun, H. Hou, F. Jiang, X. Ji, W. Zhao and Y. Hu, A process for combination of recycling lithium and regenerating graphite from spent lithium-ion battery, *Waste Manag.*, 2019, **85**, 529–537.

26 S. Rothermel, M. Evertz, J. Kasnatscheew, X. Qi, M. Grützke, M. Winter and S. Nowak, Graphite Recycling from Spent Lithium-Ion Batteries, *ChemSusChem*, 2016, **9**(24), 3473–3484.

27 H. Wang, Y. Huang, C. Huang, X. Wang, K. Wang, H. Chen, S. Liu, Y. Wu, K. Xu and W. Li, Reclaiming graphite from spent lithium ion batteries ecologically and economically, *Electrochim. Acta*, 2019, **313**, 423–431.

28 Z. Ma, Y. Zhuang, Y. Deng, X. Song, X. Zuo, X. Xiao and J. Nan, From spent graphite to amorphous sp^2+sp^3 carbon-coated sp^2 graphite for high-performance lithium ion batteries, *J. Power Sources*, 2018, **376**, 91–99.

29 A. C. Ferrari and J. Robertson, Interpretation of Raman spectra of disordered and amorphous carbon, *Phys. Rev. B: Condens. Matter Mater. Phys.*, 2000, **61**(20), 14095–14107.

30 A. C. Ferrari and D. M. Basko, Raman spectroscopy as a versatile tool for studying the properties of graphene, *Nat. Nanotechnol.*, 2013, **8**(4), 235–246.

31 F. Tuinstra and J. L. Koenig, Raman Spectrum of Graphite, *J. Chem. Phys.*, 1970, **53**(3), 1126–1130.

32 W. Ling, Z.-A. Wang, Q. Ma, Q. Deng, J.-F. Tang, L. Deng, L.-H. Zhu, X.-W. Wu, J.-P. Yue and Y.-G. Guo, Phosphorus and oxygen co-doped composite electrode with hierarchical electronic and ionic mixed conducting networks for vanadium redox flow batteries, *Chem. Commun.*, 2019, **55**(77), 11515–11518.

33 K. Yamazaki, Y. Maehara and K. Gohara, Characterization of TEM moiré patterns originating from two monolayer graphenes grown on the front and back sides of a copper substrate by CVD method, *J. Phys. Soc. Jpn.*, 2018, **87**(6), 061011.

34 H.-K. Jeong, Y. P. Lee, R. J. W. E. Lahaye, M.-H. Park, K. H. An, I. J. Kim, C.-W. Yang, C. Y. Park, R. S. Ruoff and Y. H. Lee, Evidence of graphitic AB stacking order of graphite oxides, *J. Am. Chem. Soc.*, 2008, **130**(4), 1362–1366.

35 W. S. Kim, S. Y. Moon, H. J. Kim, S. Park, J. Koyanagi and H. Huh, Large-scale graphene-based composite films for flexible transparent electrodes fabricated by electrospray deposition, *Mater. Res. Express*, 2014, **1**(4), 046404.

36 X. Li, L. Basile, B. Huang, C. Ma, J. Lee, I. V. Vlassiouk, A. A. Puretzky, M.-W. Lin, M. Yoon and M. Chi, Van der Waals epitaxial growth of two-dimensional single-crystalline GaSe domains on graphene, *ACS Nano*, 2015, **9**(8), 8078–8088.

37 T. Ohzuku, Y. Iwakoshi and K. Sawai, Formation of lithium-graphite intercalation compounds in nonaqueous electrolytes and their application as a negative electrode for a lithium ion (shuttlecock) cell, *J. Electrochem. Soc.*, 1993, **140**(9), 2490–2498.

38 T. Aida, K. Yamada and M. Morita, An Advanced Hybrid Electrochemical Capacitor That Uses a Wide Potential Range at the Positive Electrode, *Electrochem. Solid-State Lett.*, 2006, **9**(12), A534–A536.

39 K. Persson, V. A. Sethuraman, L. J. Hardwick, Y. Hinuma, Y. S. Meng, A. Van Der Ven, V. Srinivasan, R. Kostecki and G. Ceder, Lithium diffusion in graphitic carbon, *J. Phys. Chem. Lett.*, 2010, **1**(8), 1176–1180.

40 J. J. Ren, L. W. Su, X. Qin, M. Yang, J. P. Wei, Z. Zhou and P. W. Shen, Pre-lithiated graphene nanosheets as negative electrode materials for Li-ion capacitors with high power and energy density, *J. Power Sources*, 2014, **264**, 108–113.

41 P. Sennu, V. Aravindan, M. Ganesan, Y.-G. Lee and Y.-S. Lee, Biomass-Derived Electrode for Next Generation Lithium-Ion Capacitors, *ChemSusChem*, 2016, **9**, 849–854.

42 V. Khomenko, E. Raymundo-Piñero and F. Béguin, High-energy density graphite/AC capacitor in organic electrolyte, *J. Power Sources*, 2008, **177**(2), 643–651.

43 V. Aravindan, S. Jayaraman, F. Tedjar and S. Madhavi, From Electrodes to Electrodes: Building High-Performance Li-Ion

Capacitors and Batteries from Spent Lithium-Ion Battery Carbonaceous Materials, *ChemElectroChem*, 2019, **6**(5), 1407–1412.

44 H. Dai, B. Jiang and X. Wei, Impedance Characterization and Modeling of Lithium-Ion Batteries Considering the Internal Temperature Gradient, *Energies*, 2018, **11**(1), 220.

45 N. El Ghossein, A. Sari and P. Venet, Nonlinear Capacitance Evolution of Lithium-Ion Capacitors Based on Frequency and Time Domain Measurements, *IEEE Transactions on Power Electronics*, 2017, p. 1.

46 X. Gao, C. Zhan, X. Yu, Q. Liang, R. Lv, G. Gai, W. Shen, F. Kang and Z.-H. Huang, A High Performance Lithium-Ion Capacitor with Both Electrodes Prepared from Sri Lanka Graphite Ore, *Materials*, 2017, **10**(4), 414.

47 Y. Firouz, N. Omar, J. M. Timmermans, P. Van den Bossche and J. Van Mierlo, Lithium-ion capacitor – Characterization and development of new electrical model, *Energy*, 2015, **83**, 597–613.